LA-7522-MS
Informal Report

C.3

Fiber-Reinforced Plastic-Bonded Explosives

LOS ALAMOS SCIENTIFIC LABORATORY
Post Office Box 1663 Los Alamos, New Mexico 87545

This work was performed for the Iowa Army Ammunition Plant, with funds provided under Mason & Hanger-Silas Mason Co., Inc., Purchase Order 92371.

UNITED STATES
DEPARTMENT OF ENERGY
CONTRACT W-7405-ENG. 36

LA-7522-MS
Informal Report

Special Distribution
Issued: October 1978

Fiber-Reinforced Plastic-Bonded Explosives

A. P. Torres
A. S. Vigil

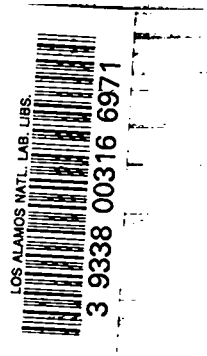

CONTENTS

	ABSTRACT	1
I.	INTRODUCTION	2
II.	PRELIMINARY SAFETY TESTS	3
	A. Thermal Stability	3
	B. Vacuum Stability	3
	C. Drop Weight Impact Sensitivity	3
III.	RAW MATERIALS USED IN THE PREPARATION OF X-0308 AND X-0312	4
	A. RDX	4
	B. Estane 5703 F-1	4
	C. Polyethylene Fibers	4
	D. Silane A-186 Additive	4
IV.	PBX PROCESSING	4
	A. Molding Powder Preparation	4
	B. Charge Preparation	5
V.	DETONATION AND INITIATION CHARACTERISTICS	5
	A. Detonation Velocity	6
	B. Small-Scale Gap Sensitivity	6
VI.	PHYSICAL PROPERTIES	6
VII.	THERMAL STRESS ANALYSIS	7
	A. Experimental	7
	B. Thermal and Stress Calculations	8
	1. Bare HE Test Calculations	9
	2. M-73 Mine Test Calculations	10
	3. Calculation of Confined Configuration	11
VIII.	CONCLUSION	12
IX.	REFERENCES	12
	TABLE I - VACUUM STABILITY OF X-0308 AND X-0312	13

TABLE II - DROP WEIGHT IMPACT SENSITIVITY 13

TABLE III - PREPARATION OF X-0308 AND X-0312 MOLDING POWDER 14

TABLE IV - DETONATION VELOCITY COMPARISON 16

TABLE V - SMALL-SCALE GAP SENSITIVITY 16

TABLE VI - PHYSICAL PROPERTIES OF X-0308 AND X-0312 17

TABLE VII - THERMAL CYCLE MODELING/TEST RESULTS 18

TABLE VIII - MATERIAL PROPERTIES USED BY TSAAS 23

Fig. 1. X-0308, DTA, and pyrolysis data. 24
Fig. 2. X-0312, DTA, and pyrolysis data. 24
Fig. 3. X-0308 pressing evaluation. 25
Fig. 4. X-0312 pressing evaluation. 25
Fig. 5. Antitank mine with main explosive charge dimensions. 25
Fig. 6. Unconfined thermal test (temperature cycle: 74°C to -54°C to 25°C). 26
Fig. 7. Confined thermal test (temperature cycle: 74°C to -54°C to 25°C). 27
Fig. 8. Finite element mesh of antitank mine. 28
Fig. 9. Finite element mesh of full antitank mine. 28
Fig. 10. Material boundaries of antitank mine. 28
Fig. 11. Temperature gradients in unconfined configuration. 29
Fig. 12. Circumferential stress contours in X-0280. 29
Fig. 13. Radial stress contours in X-0280. 30
Fig. 14. Circumferential stress contours in X-0308. 30
Fig. 15. Circumferential stress contours in X-0312. 31
Fig. 16. X-0280 temperature gradients in confined configuration. 31
Fig. 17. Circumferential stress contours in X-0280. 32
Fig. 18. Circumferential stress contours in X-0308. 32
Fig. 19. Circumferential stress contours in X-0312. 33
Fig. 20. Radial stress contours in X-0280. 33
Fig. 21. Radial stress contours in X-0308. 34
Fig. 22. Radial stress contours in X-0312. 34
Fig. 23. Temperature gradients in confined configuration with unbonded cover. 35
Fig. 24. Circumferential stress contours in X-0280. 35
Fig. 25. Circumferential stress contours in X-0308. 36
Fig. 26. Circumferential stress contours in X-0312. 36
Fig. 27. Radial stress contours in X-0280. 37
Fig. 28. Radial stress contours in X-0308. 37
Fig. 29. Radial stress contours in X-0312. 38

FIBER-REINFORCED PLASTIC-BONDED EXPLOSIVES

by

A. P. Torres
A. S. Vigil

ABSTRACT

Fiber reinforcement in plastic-bonded explosives was studied to determine the ability of fiber reinforcement to reduce munition main charge cracking under a severe thermal cycle. Two fiber-reinforced plastic-bonded explosives, X-0308 (95 wt% RDX, 4.5 wt% Estane, 0.5 wt% polyethylene fibers) and X-0312 (95 wt% RDX, 3.5 wt% Estane, 1.5 wt% polyethyelene fibers), were evaluated and compared against their nonfiber-reinforced homolog, X-0280 (95 wt% RDX, 5 wt% Estane).

Experimentation on X-0280, X-0308, and X-0312 under various cycle combinations of 74, -54, and 25°C was performed. Pieces molded from X-0308 and X-0312 gave similar results: they formed closed, hairline, radial cracks. In contrast, pieces of X-0280 developed large, open cracks and broke in half under light hand pressure. Sensitivity and thermal stability of X-0308 and X-0312 were similar to X-0280. Because of their identical high-explosive composition, energy and detonation pressures of X-0308 and X-0312 were expected to be similar to their homolog. Detonation tests on X-0312, the molding powder with the highest fiber content, showed it to be similar to X-0280. Procedures for the preparation of the fiber-reinforced molding powders were similar to X-0280, but require an additive, Silane A-186, for full incorporation of the fibers.

A thermal stress analysis was done to provide insight to the experimental results. TSAAS, a two-dimensional, finite element thermal- and stress-analysis code, was used. Predictions corresponded closely with experimental results. The study demonstrated that fiber incorporation above 0.5 wt% did not improve resistance to cracking.

I. INTRODUCTION

The development of a new high-explosive material for use in munitions includes the qualification of the new explosive and the munition. The properties of the explosive must be known so that the munition can be designed properly. To qualify the explosive for use, a variety of tests must be performed in accordance with established procedures.[1]

The work described in this report was performed for the Iowa Army Ammunition Plant (IAAP) to provide data on a replacement explosive for use in the artillery-dispersed, antitank mine now being developed at Army Armament Research and Development Command, Dover, NJ. One requirement is that the assembled mine must pass a harsh thermal-cycle test (heated to 74°C and then shock-cooled to -54°C). When assembled mines were subjected to this test, the current explosive fill, Los Alamos Scientific Laboratory (LASL) formulation X-0280 (95 wt% RDX, 5 wt% Estane), cracked severely.

Because the mine is to be artillery dispersed, there is concern about in-bore premature ignition. One possible mechanism for in-bore premature initiation of the explosive fill is the generation and transport of thermal energy from closure of a gap or crack in the fill. The forces imposed on the explosive fill during launch tend to close the gap, heat the gas in the void, and initiate a decomposition reaction in the explosive. Because X-0280 fractured with large, open cracks when subjected to thermal-cycle tests conducted at IAAP, it became necessary to investigate means to reduce the tendency to form large, open cracks and thus the probability of premature ignition within the mine. A more desirable mode of fracture would be the formation of small, closed

cracks rather than large, open cracks. Therefore, one feasible approach was to develop an explosive that fails in many small cracks rather than a few large cracks when exposed to the required thermal cycle.

It is known that plastics and explosives can be reinforced with fibers with a resulting increase in the tensile strength. Apparently, the failure mechanism is changed, and instead of failing with large, open cracks, the material yields with many small, closed cracks. The objective of this work was to determine the effects of incorporating plastic fibers in X-0280 and to supply fiber-reinforced molding powder to IAAP for evaluation in munitions.

Two plastic-bonded explosive formulations were studied: X-0308 (95 wt% RDX, 4.5 wt% Estane, 0.5 wt% polyethylene fibers) and X-0312 (95 wt% RDX, 3.5 wt% Estane, 1.5 wt% polyethylene fibers).

II. PRELIMINARY SAFETY TESTS

LASL performs a series of preliminary safety tests before working with new explosive formulations or with explosives that have not been used by LASL. The results of these tests are used to assess the safety characteristics of the explosive and to guide the selection of operating procedures and handling techniques. A minimum evaluation includes a measure of thermal stability and impact sensitivity.

A. Thermal Stability

The differential thermal analysis (DTA) and pyrolysis curves for X-0308 and X-0312 are presented in Figs. 1 and 2. These curves exhibit no unusual exotherm or gas evolution.

B. Vacuum Stability

Vacuum stability tests were conducted at 120°C for 48 h. The data are shown in Table I. The total gas evolved from the test samples is another measure of thermal stability. The amount of gas evolved for X-0308 and X-0312 is typical for plastic-bonded RDX.

C. Drop Weight Impact Sensitivity

The drop weight impact sensitivity test was performed by using a Naval Ordnance Laboratory (NOL) standard impact machine with a 2.5-kg weight.[2] The results of this test, shown in Table II, indicate that X-0308 and X-0312 are moderately sensitive PBXs.

III. RAW MATERIALS USED IN THE PREPARATION OF X-0308 AND X-0312

The X-0308 and X-0312 formulations are homologs of the X-0280 formulation. RDX content was held at 95 wt% and plastic fibers were substituted for some of the binder (Estane) used in the X-0280 formulation.

A. RDX

The RDX used for this study was standard Holston Defense Corporation (HDC) Type B RDX. As with X-0280, a bimodal particle-size distribution, consisting of three parts of Type B, Class G RDX and one part Type B, Class E RDX, was used to enhance pressing characteristics. Both RDX classes are described in military specification MIL-R-398C.

B. Estane 5703 F-1

Estane is a proprietary (polyester-urethane) elastomer marketed by B. F. Goodrich Chemical Company. The Estane 5703 F-1 used in this study was purchased according to LASL Specification 13Y-101301.

C. Polyethylene Fibers

The polyethylene fibers were high-density polyethylene (melting point of 121°C), machine cut to a fiber length of 2.5 mm. The fibers were nominally 25 μm in diameter. The fibers were obtained from Mini Fibers, Inc., Weber City, VA, and were received in a mat form.

D. Silane A-186 Additive

Silane A-186 is an epoxyalkylsilane ester (chemical name: beta-(3,4 epoxycyclohexyl/ethyltrimethoxysilane) marketed by Union Carbide Corporation. This additive promotes incorporation of the fiber in the PBX.

IV. PBX PROCESSING

A. Molding Powder Preparation

Both X-0308 and X-0312 molding powders were produced by using a modified water-slurry process. The RDX is initially slurried in the solvent/binder (lacquer) solution, followed by water addition. Table III presents the procedures for processing both formulations at pilot plant scale. Methyl ethyl ketone (MEK) was used for the lacquer, because it is an excellent solvent for Estane. Although RDX is slightly soluble in MEK, the combination of the Estane, the fibers, and the additive Silane A-186 apparently reduces the solubility of RDX in MEK. Chemical analyses of processed batches of these PBXs showed no evidence of free RDX in the product.

During the initial process development for fiber incorporation, we investigated both the polyethylene fiber and a Dacron fiber. We elected to continue development with polyethylene fibers. The polyethylene remains in full suspension in the lacquer, which allows optimum homogeneity with RDX under agitation. Dacron is more difficult to keep in suspension, which results in vessel-bottom fouling and poorer product yield.

We found a restriction in the length of fibers that can be incorporated in the PBX. Fibers 6 mm long resulted in poor incorporation in the PBX and severe vessel fouling. Fibers of that length would mass adhere around the agitator shaft. We found that a 2.5-mm fiber length would incorporate fully in the PBX.

Three solvent removal procedures were tried with X-0308 and X-0312 processing, and all were successful. Solvent was removed by solvent extraction with additional water, by atmospheric distillation, or by vacuum distillation. We selected solvent extraction, because this method requires the least amount of processing time and energy. However, a large-scale production facility might require a separate stripping process for the batch effluent to remove MEK from water, if extraction is to be used.

The fiber-reinforced PBXs were manufactured in 90.8-kg batches in a 760-ℓ slurry vessel with a 5-hp motor. A review of processing variables should be made before scaling to larger quantities of either of the fiber-reinforced PBXs. The equipment design may well affect processing.

B. Charge Preparation

The standard method of preparing charges of PBX is by pressing and then machining these pieces into the desired configuration. In our pressing cycle, the powder was preheated, placed in a steel die, subjected to a vacuum cycle, and pressed. Figures 3 and 4 show the pressed densities obtained with X-0308 and X-0312 as a function of pressing conditions. Charges of X-0308 and X-0312 were generally pressed at 100°C, 137.9 MPa (20 000 psi), and triple intensification.

V. DETONATION AND INITIATION CHARACTERISTICS

Because the compositions and densities of X-0280, X-0308, and X-0312 are so similar, we expected the detonation properties of these explosives to vary only slightly. Consequently, the detonation velocity and small-scale gap sensitivity were determined only for X-0312, the formulation with the greatest

fiber content. The data obtained are compared with corresponding values for X-0280 in Tables IV and V.

A. Detonation Velocity

The detonation velocity of X-0312 was measured in a 25.4-mm-diam rate stick. The rate stick consisted of six 51-mm-long specimens. Each segment was instrumented with ionization pins.

The detonation velocity of X-0312 was found to be 57 m/s faster than that of X-0280. This is a slightly larger difference than expected. Calculations indicate that the difference in void content in the two rate sticks should cause an increase of about 25 m/s in the X-0312. Inclusion of the polyethylene in the binder phase should account for another approximately 20 m/s increase. The unexplained difference is then 12 m/s, which is probably within experimental error. We expect the detonation velocity of X-0308 to be about 8510 m/s at 1.740 g/cm^3.

B. Small-Scale Gap Sensitivity

The gap test gives a measure of the shock sensitivity of an explosive. In the LASL small-scale gap test, the acceptor sample is a pressed pellet 12.7 mm in diameter and 38.1 mm long. The donor is a modified SE1 detonator with a PBX 9407* pellet that is 7.6 mm in diameter and 5.3 mm long. The measured gap between the acceptor and donor is filled with brass spacer shims. In general, the larger the spacer gap, the more shock sensitive the explosive. Detonation of the acceptor is determined by the dent produced in a steel witness plate.

X-0312 gap sensitivity was shown to be slightly less than that of PBX X-0280. The difference in void content surely accounts for this difference. Table V lists data for X-0312, X-0280, and several other explosives for comparison. Based on past experience, and the present experimental data, we expect no significant difference in the shock sensitivity of X-0280, X-0308, and X-0312.

VI. PHYSICAL PROPERTIES

The elastic modulus, proportional limit, and ultimate strength of X-0308 and X-0312 were determined at -54, 25, and 74°C in both tension and compression.

*94 wt% RDX, 6 wt% Exon 461.

The linear coefficient of thermal expansion was determined over the range of -54 to 74°C. Results are given in Table VI, as are the reported properties for X-0280.

The decrease in physical strength under tension for both fiber-reinforced materials is due to the smaller content of elastomer. Their moduli show that the fiber-reinforced materials are not as stiff as X-0280. Hence, these fiber-reinforced materials are more suitable for the thermal-cycle environment.

VII. THERMAL STRESS ANALYSIS

Experiments on specimens of X-0280, X-0308, and X-0312 that were machined to the contour of the main charge for the antitank mine (Fig. 5) were performed at various thermal cycles of the 74, 25, and -54°C environments. The temperature environments for the experimental testing were controlled by a steam oven set at 74°C, a freezer set at -54°C, and the test bay room temperature set at 25°C.

A thermal stress analysis was done to provide insight into the experimental results and to predict the temperatures and stresses in the explosives during thermal cycling of real mines. TSAAS,[3] a two-dimensional, finite element thermal- and stress-analysis code was used in the calculations.

A. Experimental

The X-0280, X-0308, and X-0312 specimens were each subjected to various thermal cycle combinations of 74, 25, and -54°C temperatures. The specimens were tested under several degrees of confinement: no confinement (bare explosive); full confinement (complete mine assembly); or the explosive with a stainless steel plug in place of the S&A assembly.

During the tests, at different thermal cycles and all degrees of confinement, crack-generation rate was uniform for the three formulations. If the specimens were initially held at a temperature above -54°C and then cooled to -54°C, there was no evidence of cracks with any of the three formulations. The only time that the specimens cracked was when they were removed from the -54°C environment and allowed to warm up. Specimen cracking for all formulations was not gradual while warming from -54°C, but rapid--within 1 to 2 minutes after removal from -54°C.

The crack patterns were material dependent throughout testing at all stages of confinement. X-0308 and X-0312 gave identical results. Each fractured with closed, hairline cracks that started radially from the center and

extended to a length equal to 3/4 of the outer surface length from the center. In contrast, X-0280 fractured with large, open cracks, extending over the entire surface. With light hand pressure, the X-0280 specimens broke in half.

The thermal cycle for the unconfined tests was an initial equilibration at 74°C, sudden exposure to -54°C, equilibration at -54°C, and then removal for warming to 25°C. X-0308 and X-0312 gave closed, hairline cracks. X-0280 cracked and separated in two pieces upon handling. Therefore, the temperature gradient imposed during warming from -54°C inside the main explosive charge is a primary contributor to material failure; the metal confinement from the mine cannot be considered to be the only cause for main charge cracking under a thermal cycle.

Possibly a design change in the main charge face curvature to allow for thicker explosive could enhance material physical integrity. The suggested design change could make use of the fact that the cracks started at the minimum thickness of the main charge (at the center) and ended at that thickness of the main charge (approximately 38 mm) corresponding to 3/4 of the outer surface length from the center.

Table VII lists the various test cycles and results for the three materials. Figures 6 and 7 show examples of the test specimens after cycle testing.

B. Thermal and Stress Calculations

In the finite element method, the continuous solid is replaced by a system of ring elements with triangular or quadrilateral cross sections. Two finite element meshes of the antitank mine were made for use by the TSAAS code to analyze the explosive charge under (1) no confinement (bare charge), (2) full confinement (complete, fully bonded, mine assembly), and (3) confinement with the top cover not bonded to the explosive. The tests done with the stainless steel plug glued in the charge centerbore were not analyzed. The finite element mesh shown in Fig. 8 was used to do the calculations for both the bare charge tests and the complete, fully bonded mines. Because the units in both these configurations were axisymmetric about the Z axis, and the top and bottom halves were identical, with identical boundary conditions in the Z direction, full advantage could be taken of the symmetry in setting up the problem. The local confined tests were done with all mine components bonded together, except for the steel cover, which was left unbonded to allow inspection of the thermally cycled specimens. Because of this, the test boundary conditions were not

symmetric in the Z direction, and the calculations of the confined tests were done by using the finite element mesh of a full unit shown in Fig. 9. Figure 9 also shows the limited tension layer used to simulate the unbonded explosive steel cover interface. The limited tension layer, as used in TSAAS, reduces the modulus of the material by 1000 if the stress in the axial direction exceeds a small positive value.

The material boundary outline of the mine specimens, showing the specimen components, is shown in Fig. 10. The S&A assembly and the booster explosive in the antitank mine were replaced by an aluminum plug and an extension of the explosive, respectively. The material properties used by TSAAS are listed in Table VIII. The mechanical properties of the explosives at temperatures of -54, 25, and 74°C were used because they are highly temperature dependent. But, because the mechanical properties of the metals used in the tests exhibit only a slight temperature dependence, only their room-temperature properties were used in the calculations.

The results of the calculations indicate that, as expected, the explosive in the full mine assembly is under compression when the mine is allowed to reach an equilibrium temperature higher than the assumed assembly temperature of 25°C. Even at the maximum allowed equilibrium temperature of 74°C, there is little danger of damage to the explosive under compression because its compressive strength is many times greater than its tensile strength. Therefore, we need only concern ourselves with the explosive under tension, which occurs when (1) the mine is being cooled to its lowest allowable temperature of -54°C, (2) it is allowed to equilibrate at -54°C, or (3) it is being heated from the -54°C equilibrium temperature.

1. Bare HE Test Calculations. The calculations were done on the unconfined configuration using the mesh shown in Fig. 8 by reducing the elastic moduli of the materials surrounding the explosive to 0.1 MPa to eliminate the effects of the aluminum and steel components. There is no stress in the unconfined configuration if it is in a state of thermal equilibrium, regardless of the temperature, because the coefficient of thermal expansion is the same throughout the unit. We calculate a high tensile stress in the explosive when it is being cooled to -54°C, zero stress when it is allowed to equilibrate at -54°C, and the maximum tensile stress when it is being heated from the -54°C equilibration temperature. A temperature boundary condition of 25°C was set

at the exterior surfaces of the mine, and heat was allowed to flow into the explosive to simulate the unconfined unit being taken out of a -54°C environment and into a room at 25°C. The maximum stresses calculated in the unconfined units occur approximately 3 min after the start of the heating cycle from the equilibrium temperature of -54°C. Figure 11 shows the isotherms when the calculated circumferential stress in the X-0280 is at its peak. The circumferential stress contours in the X-0280 are shown in Fig. 12 and, for comparison, the radial stress contours are shown in Fig. 13. Negative values denote compression, and positive values denote tension. The tensile stresses are highest where the temperatures are the lowest, and the circumferential stress is the highest stress calculated for the unconfined configuration. Figures 14 and 15 show the circumferential stress contours in the fiber-reinforced explosives at the time when the stresses are at their peak. By comparing Figs. 12, 14, 15, and the data in Table VIII, one notes that all the peak stresses are several times greater than the ultimate strengths of the explosives, and the maximum stress in the X-0280 is more than twice as great as the maximum stress in the X-0308 and X-0312. This is consistent with test observations, because radial hairline cracks were detected in the fiber-reinforced test specimens, and the X-0280 test specimen broke in two when allowed to warm up from the -54°C equilibrium temperature.

2. M-73 Mine Test Calculations. The calculations done on the complete M-73 antitank mine configuration, with the explosive bonded to the steel and aluminum components, indicate that the circumferential stress is the maximum tensile stress in the explosive when the mine is at an equilibrium temperature of -54°C. The maximum circumferential stresses calculated in the X-0280, X-0308, and X-0312 materials at a temperature of -54°C were 77.5, 23.1, and 27.8 MPa, respectively, whereas the maximum radial stresses were 66.0, 21.5, and 26.2 MPa, respectively. However, the calculations indicate that the tensile stresses increase as the mine is allowed to warm up from -54°C. A temperature boundary condition of 25°C was set on the outer steel cylinder surface (the top and bottom of the explosive in the real mine are insulated by low-conductivity materials), and heat was allowed to flow into the unit to simulate the mine's being removed from a -54°C environment and allowed to warm up in a room-temperature environment. The maximum circumferential stress on the explosive occurs approximately 0.5 min after the start of the heating cycle. Figure 16 shows

the isotherms at the time when the circumferential stress in the X-0280 is at its peak. Most of the explosive is still at a temperature of -54°C at this time. The circumferential stress contours in the X-0280, X-0308, and X-0312 at the time when the stresses are at their peak are shown in Figs. 17-19, respectively. The radial stress contours in the three explosives are presented in the same order in Figs. 20-22. The peak circumferential stress in the X-0280 is greater than its peak radial stress, but the fiber-reinforced explosives, in some cases, have radial stresses that are slightly greater than their circumferential stresses. Once again, the data of Figs. 17-22 indicate peak stresses that are several times greater than the ultimate strengths of the explosives, and the maximum stress in the X-0280 is almost three times greater than in X-0312 or X-0308. There are no experimental data from a fully bonded mine because the explosive would be broken upon disassembly for post-test inspection. Hence, these calculations cannot be compared with experimental results.

3. Calculation of Confined Configuration. The calculations done on the confined configuration with the unbonded top cover, using the finite element mesh shown in Fig. 9, agree with the previous calculations. The tensile stresses increase as the unit is allowed to warm up from an equilibrium temperature of -54°C. The maximum circumferential stress on the explosive occurs approximately 0.5 min after the start of the heating cycle. In this case, a temperature boundary condition of 25°C was set on the outer steel cylinder surface and on the top surface of the inner aluminum cylinder (because this surface was exposed to the ambient air), and heat was allowed to flow into the unit to simulate a change from a -54°C environment to a 25°C environment. Figure 23 shows the isotherms at the time when the circumferential stress in the explosive is at its peak. At this time, most of the explosive, except near the exterior surfaces, is still at a temperature of -54°C. The circumferential stress contours in the X-0280, X-0308, and X-0312 at the time when the stresses are at their peaks are presented in Figs. 24-26, respectively. The radial stress contours in the three explosives are shown in the same order in Figs. 27-29. The figures indicate that the maximum circumferential stresses in the X-0280, X-0308, and X-0312 are 88.3, 27.9, and 33.1 MPa, respectively. Excluding the top left-hand corner, the maximum radial stresses in the explosives (in the same order) are 67.1, 23.4, and 30.5 MPa. The circumferential stresses exceed the radial stresses at all points in all three explosives except for the top left-hand corner.

The radial stresses in the top left-hand corner are twice as high as anywhere else in the explosive and much greater than the peak circumferential stresses. Test observations provided no evidence of cracking caused by radial stress in the top left-hand corner of the test specimens. However, the rest of the calculational data are consistent with test observations, because radial hairline cracks were detected on the surface of the X-0308 and X-0312, and open radial cracks were found extending over the entire length of the surface of the X-0280 when the specimens were allowed to warm up from -54°C.

The calculational results obtained in this analysis are included in Table VII for comparison with the experimental findings. In each case, the calculated stress in the explosive greatly exceeds its yield stress, indicating possible failure even at less severe thermal environments than existed in the tests, but the relative magnitudes agree well with the observed results. The peak stresses calculated with TSAAS occur at the point in the thermal cycle when the cracking was observed, and the cracks were in the radial direction as predicted.

VIII. CONCLUSION

Throughout the entire testing program, X-0308 and X-0312 behaved the same. The calculated values obtained from the thermal stress modeling also show the similarity in behavior between the two materials. The incorporation of polyethylene fibers at the 0.5 wt% level does not prevent cracking under a severe thermal cycle environment, but does reduce the cracks to hairline size. Incorporation of polyethylene fibers at higher levels does not provide any additional benefit.

We recommended that X-0308 be considered as a replacement for X-0280 in the mine if the intent is to replace large open cracks with fine hairline cracks.

IX. REFERENCES

1. "Safety and Performance Tests for Qualification of Explosives," Naval Ordnance Systems Command Report NAVORD-OD-44811, Vol. 1 (January 1, 1972).

2. G. R. Walker, E. C. Whitbread, and D. C. Hornig, "Manual of Sensitiveness Tests" (US/Impact/03) CARDE, TTCP Panel O-2 (February 1966).

3. R. V. Browning, D. G. Miller, and C. A. Anderson, "TSAAS: Finite Element Thermal and Stress Analysis of Axisymmetric Solids with Orthotropic Temperature-Dependent Material Properties," Los Alamos Scientific Laboratory report LA-5599-MS (May 1974).

TABLE I

VACUUM STABILITY OF X-0308 AND X-0312

Material	Gas Evolution (48 h at 120°C, ml/g @ STP)
X-0308	0.4
X-0312	0.2
X-0280	0.4
LX-14[a]	0.4
RDX	0.2
HMX	0.2

[a]95 wt% HMX, 5 wt% Estane 5703 F-1.

TABLE II

DROP WEIGHT IMPACT SENSITIVITY

(2.5-kg drop weight, NOL machine)

Material	Sensitivity (50% height, cm) Type 12	Type 12B
X-0308	45	42
X-0312	42	52
X-0280	51	43
LX-14	52	58
RDX	22	30
HMX	26	33

TABLE III

PREPARATION OF X-0308 AND X-0312 MOLDING POWDER

I. FORMULATION

A. X-0308

Desired composition by weight: 95 wt% RDX, 4.5 wt% Estane, 0.5 wt% polyethylene fibers.

Formulation

RDX:	21.6 kg	Type B, Class E
	64.7 kg	Type B, Class G
	86.3 kg	total
Lacquer:	4.1 kg	Estane 5703 F-1
	0.4 kg	polyethylene fibers
	4.5 kg	total inert with 136.2 g Silane A-186, dispersed in 36.3 kg of MEK

B. X-0312

Desired composition by weight: 95 wt% RDX, 3.5 wt% Estane, 1.5 wt% polyethylene fibers.

Formulation

RDX:	21.6 kg	Type B, Class E
	64.7 kg	Type B, Class G
	86.3 kg	total
Lacquer:	3.1 kg	Estane 5703 F-1
	1.4 kg	polyethylene fibers
	4.5 kg	total inert with 272.4 g Silane A-186, dispersed in 36.3 kg of MEK

TABLE III continued

II. PROCEDURE

1. Slurry RDX in lacquer at room temperature and low agitation.
2. Add 182 kg of water at room temperature.
3. Solvent removal: any one of the three following procedures may be used.
   a. Solvent Extraction:
      (1) Heat slurry to 60°C.
      (2) Add 136 kg of water at room temperature and allow to cool to 35°C.
      (3) Flood vessel with water and dump onto a filter. Wash filtrate with cold water.
   b. Vacuum Distillation:
      (1) Heat slurry to 60°C.
      (2) Add 136 kg of water at room temperature.
      (3) Vacuum distill MEK/water azeotrope over temperature range of 35 to 45°C.
      (4) Dump onto a filter and wash with cold water.
   c. Atmospheric Distillation:
      (1) Heat slurry to 65°C.
      (2) Distill azeotrope over temperature range of 65 to 93°C.
      (3) Cool and dump onto filter.
      (4) Wash with cold water.
4. Vacuum dry molding powder at 65°C.

TABLE IV

DETONATION VELOCITY COMPARISON

Material	Density (g/cm^3)	Detonation Velocity (m/s)
X-0312[a]	1.739	8525
X-0280[b]	1.740	8468

TABLE V

SMALL-SCALE GAP SENSITIVITY

Material	Density (g/cm^3)	% Voids	Mean Gap (mm brass)	M_{95}
X-0312	1.738	0.9	1.57	±0.36
X-0280	1.737	1.5	1.70	±0.05
LX-14[c]	1.815	1.4	1.73	±0.10
Comp B-3[d]	1.721	1.8	1.30	±0.15

[a] 95 wt% RDX, 3.5 wt% Estane, 1.5 wt% polyethylene fibers.

[b] 95 wt% RDX, 5 wt% Estane.

[c] 95 wt% HMX, 5 wt% Estane.

[d] 60 wt% RDX, 40 wt% TNT.

TABLE VI

PHYSICAL PROPERTIES OF X-0308 AND X-0312

Material	Density (g/cm^3)	Coefficient of Thermal Expansion, Linear (10^{-6}/°C)	Temp. (°C)	Compression [MPa (psi)]		Tension [MPa (psi)]		Modulus [GPa (10^6 psi)]
				Proportional Limit	Ultimate Strength	Proportional Limit	Ultimate Strength	
X-0308	1.742	61.5	-54	37.6 (5445)	58.3 (8455)	2.3 (335)	2.3 (335)	3.2 (0.46)
			25	5.3 (768)	16.4 (2372)	1.6 (232)	3.3 (481)	2.4 (0.35)
			74	8.1 (1179)	9.5 (1374)	0.2 (31)	0.8 (120)	0.9 (0.14)
X-0312	1.739	62.1	-54	36.1 (5235)	57.5 (8333)	1.9 (279)	1.9 (279)	3.9 (0.56)
			25	9.8 (1422)	19.9 (2886)	1.3 (191)	3.4 (492)	3.9 (0.56)
			74	3.0 (485)	11.1 (1609)	0.4 (55)	1.2 (169)	1.5 (0.21)
X-0280	1.746	68.5	-54	22.3 (3240)	53.1 (7700)	5.2 (750)	5.2 (750)	12.6 (1.83)
			25	7.2 (1120)	18.0 (2610)	1.9 (279)	4.8 (690)	5.4 (0.78)
			74	3.8 (550)	8.8 (1280)	0.5 (70)	1.5 (220)	2.1 (0.30)

TABLE VII

THERMAL CYCLE MODELING/TEST RESULTS

Material	Temp. Cycle (°C)	Predicted Maximum Stresses (TSAAS)	Experimental Results
A. X-0280			
1. 2 specimens, unconfined	74 to -54 to 25	1. Peak stress occurs 150 s after specimen is allowed to warm from -54°C. Peak stress is 28.7 MPa (4160 psi) in the circumferential direction. Fracture to be radial.	1. No visible cracks at 74 or -54°C. Specimens cracked in half when exposed to room temperature and allowed to warm from -54°C.
2. 2 specimens, stainless steel (SS) plug bonded in centerbore	74 to -54 to 25	2. No analysis done.	2. No visible cracks at 74 or -54°C. Specimens cracked with open, radial cracks when allowed to warm up from -54°C; when handled, broke in half.
3. 2 specimens, SS plug bonded in centerbore	-54 to 74 to 25	3. No analysis done.	3. Cracks visible after removal from -54°C. No additional cracking during course of cycle.

TABLE VII continued

Material	Temp. Cycle (°C)	Predicted Maximum Stresses (TSAAS)	Experimental Results
A. X-0280			
4. Complete assembly and bonding in mine	74 to -54 to 25	4. Peak stress occurs 40 s after specimen is allowed to warm from -54°C. Peak stress is 85.1 MPa (12 300 psi) in the circumferential direction. Peak radial stress is nearly as great at 84.2 MPa (12 200 psi). Either radial or circumferential fracture expected.	4. No test made.
B. X-0308			
1. 2 specimens, unconfined	74 to -54 to 25	1. Peak stress occurs 150 s after specimen is allowed to warm from -54°C. Peak stress is 8.7 MPa (1260 psi) in the circumferential direction. Radial fracture expected.	1. No visible cracking at 74 or -54°C. Small hairline cracks when exposed to room temperature.

TABLE VII continued

Material	Temp. Cycle (°C)	Predicted Maximum Stresses (TSAAS)	Experimental Results
B. X-0308			
2. 3 specimens, bonded in mine assembly	74 to -54 to 25	2. Peak stress occurs 30 s after unit allowed to warm from -54°C. The peak stress (excluding the upper inside corner of the HE) is 27.9 MPa (4040 psi) in circumferential direction. Radial stress in upper inside corner of HE is 55.6 MPa (8060 psi).	2. Initial cycle test with specimens had side wall glue bond failure because of improper bonding technique. Specimens did not fracture at any period of cycle. Bonded specimens again to case wall and recycled. Small hairline cracks resulted after warming from -54°C. No evidence of circumferential cracking at predicted upper inside corner.
3. 2 specimens, bonded in mine assembly	-54 to 25 to 74	3. Same as 2.	3. Cracking only after removal from -54°C; small hairline cracks. No additional cracking during course of cycle.

TABLE VII continued

Material	Temp. Cycle (°C)	Predicted Maximum Stresses (TSAAS)	Experimental Results
B. X-0308			
4. 2 specimens, SS plug bonded in centerbore	74 to -54 to 25	4. No analysis done.	4. Same as 3.
5. Complete assembly and bonding in mine	74 to -54 to 25	5. Peak stress occurs 30 s after specimen is allowed to warm from -54°C. Peak stress is 26.9 MPa (3900 psi) in the radial direction. Peak circumferential stress is nearly as great at 25.5 MPa (3690 psi). Either radial or circumferential fracture expected.	5. No test made.
C. X-0312			
1. 2 specimens, unconfined	74 to -54 to 25	1. Peak stress occurs 200 s after unit allowed to warm from -54°C. Peak stress is 12.0 MPa (1740 psi) in circumferential direction. Radial fracture expected.	1. Identical results as reported for X-0308, Test B.1 above.

TABLE VII continued

Material	Temp. Cycle (°C)	Predicted Maximum Stresses (TSAAS)	Experimental Results
C. X-0312			
2. 2 specimens, bonded in mine assembly; top of mine not bonded	74 to -54 to 25	2. Peak stress occurs 40 s after unit allowed to warm from -54°C. Peak stress (excluding upper inside corner) is 33.1 MPa (4800 psi) in the circumferential direction. Maximum radial stress in upper inside corner is 72.4 MPa (10 500 psi).	2. Identical results and retest conditions as reported for X-0308, Test B.2 above.
3. 2 specimens, bonded in mine assembly; top of mine not bonded	-54 to 25 to 74	3. Same as 2.	3. Identical results as reported for X-0308, Test B.3 above.
4. Complete assembly and bonding in mine	74 to -54 to 25	4. Peak stress occurs 40 s after specimen is allowed to warm from -54°C. Peak stress is 32.1 MPa (4660 psi) in the radial direction. Peak circumferential stress is nearly as great at 31.5 MPa (4570 psi). Either radial or circumferential fracture expected.	4. No test made.

TABLE VIII

MATERIAL PROPERTIES USED BY TSAAS

Material	Density (g/cm^3)	Poisson's Ratio	Coefficient of Thermal Expansion ($\times 10^{-6}$ °C)	Temp. (°C)	Specific Heat (cal g^{-1} °C)	Thermal Conductivity (cal s^{-1} cm^{1} $°C^{-10}$)	Modulus (GPa)	Tensile Yield Stress (MPa)
Steel	7.9	0.23	13	25	0.12	0.065	193.0	242.0
Aluminum	2.8	0.35	22	25	0.213	0.39	69.0	276.0
X-0308	1.74	0.32	62	-54	0.25	0.00051	3.2	2.3
				25	0.25	0.00051	2.4	3.3
				74	0.25	0.00051	0.9	0.8
X-0312	1.74	0.32	62	-54	0.25	0.00051	3.9	1.9
				25	0.25	0.00051	3.9	3.4
				74	0.25	0.00051	1.5	1.2
X-0280	1.74	0.32	62	-54	0.25	0.00051	12.6	5.2
				25	0.25	0.00051	5.4	4.8
				74	0.25	0.00051	2.1	1.5

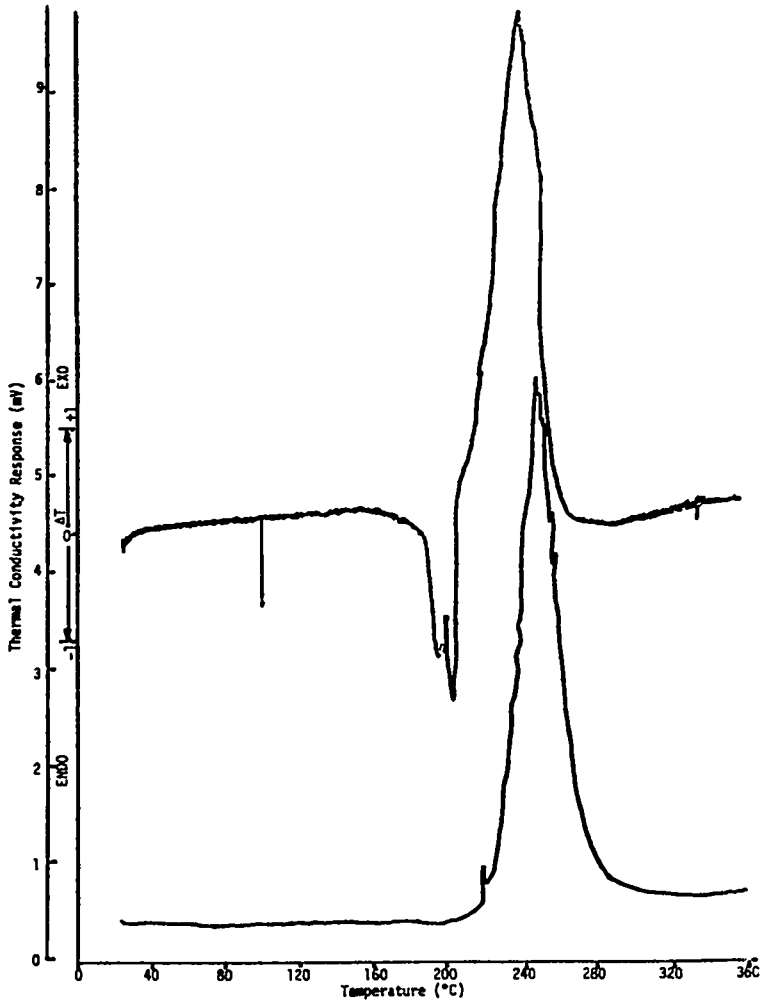

Fig. 1. X-0308, DTA, and pyrolysis data.

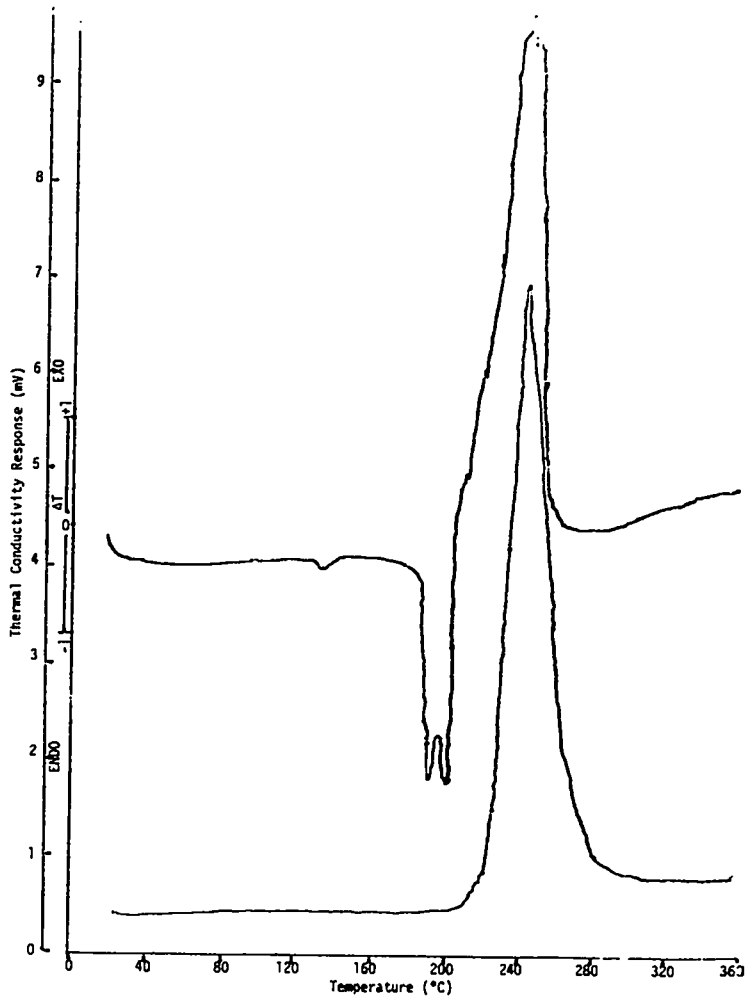

Fig. 2. X-0312, DTA, and pyrolysis data.

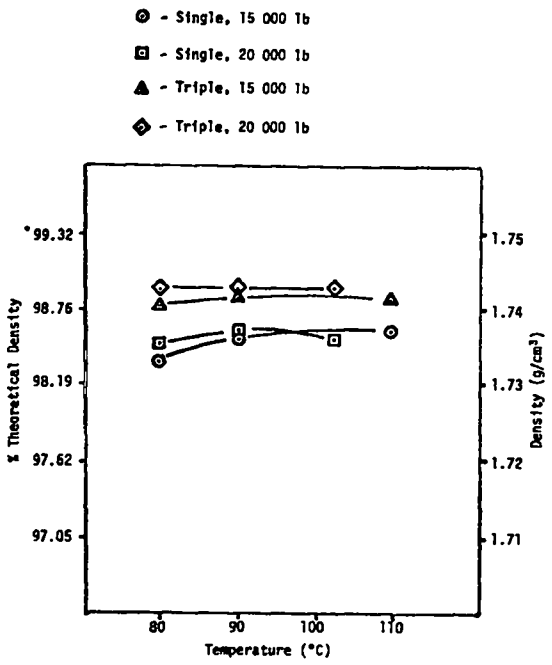

Fig. 3. X-0308 pressing evaluation.

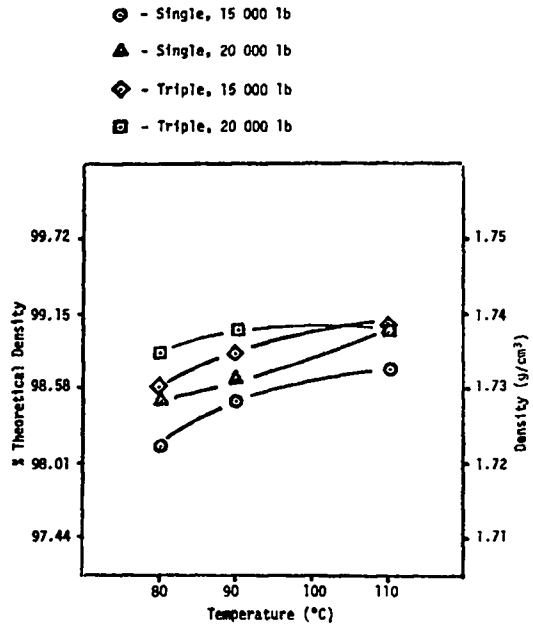

Fig. 4. X-0312 pressing evaluation.

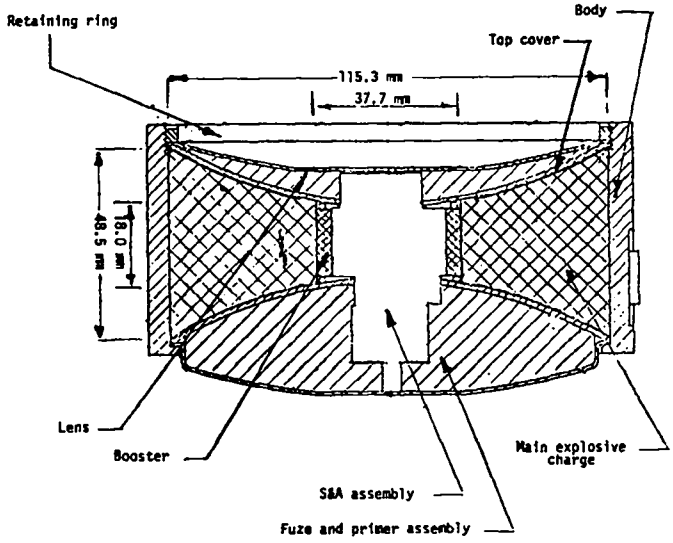

Fig. 5. Antitank mine with main explosive charge dimensions.

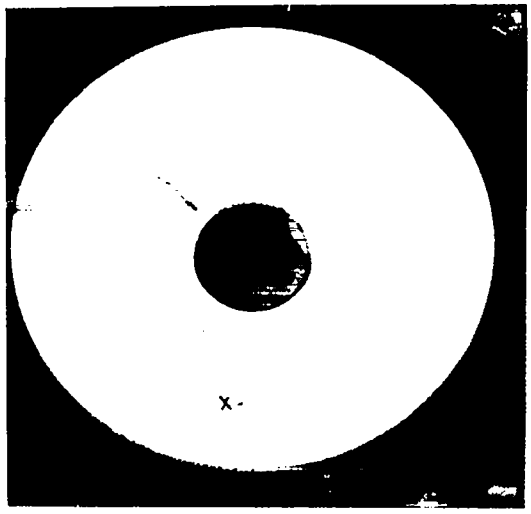

X-0312

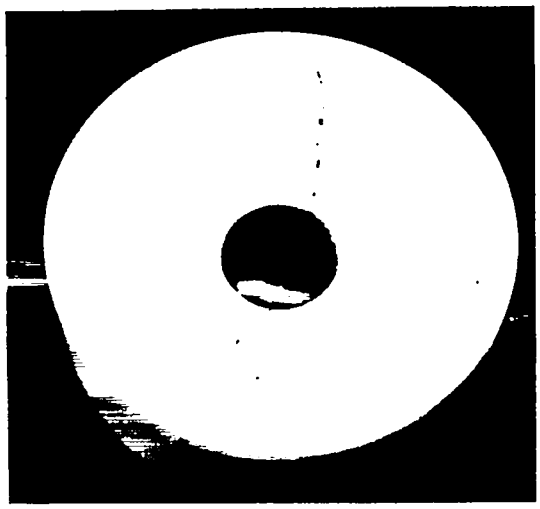

X-0308

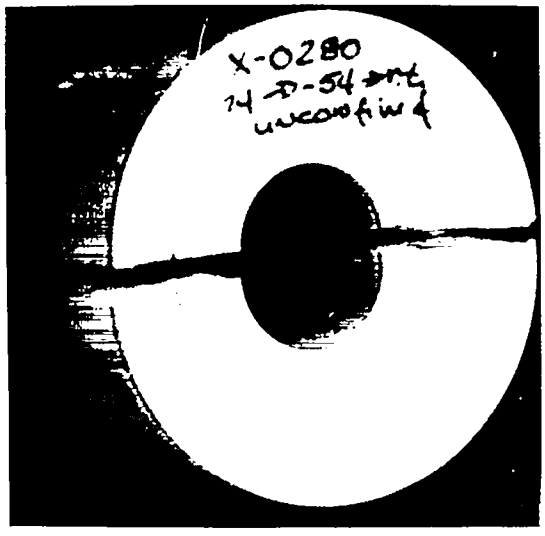

X-0208

Fig. 6. Unconfined thermal test (temperature cycle: 74°C to -54°C to 25°C).

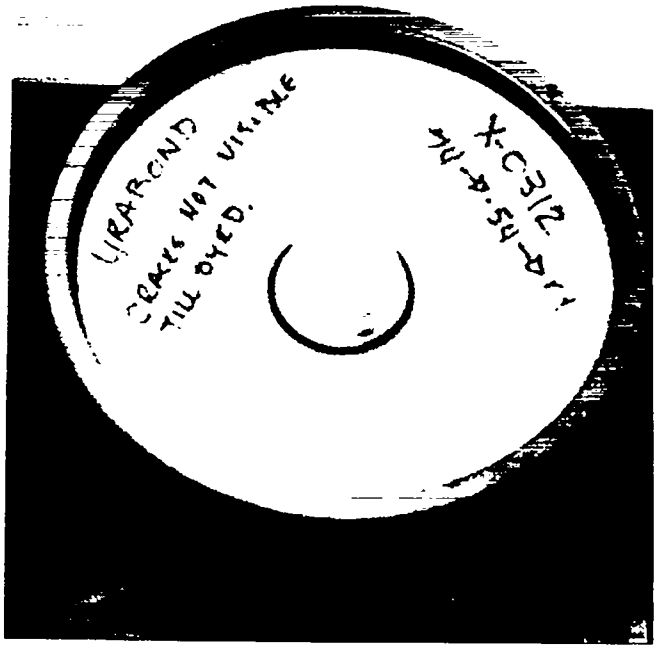

X-0312

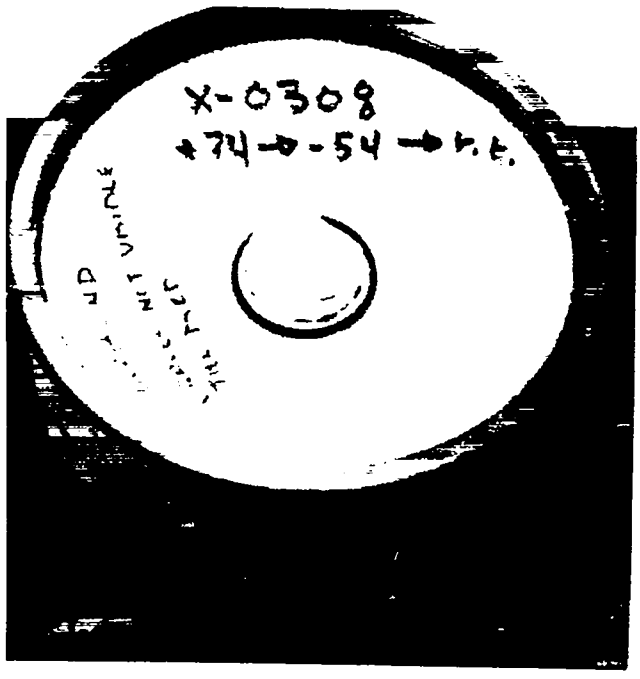

X-0308

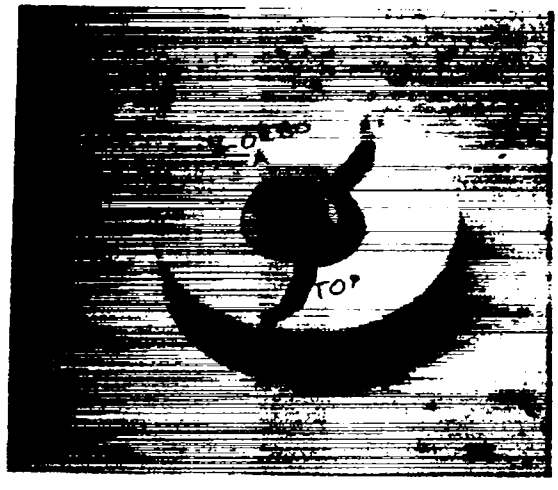

X-0280

Fig. 7. Confined thermal test (temperature cycle: 74°C to -54°C to 25°C).

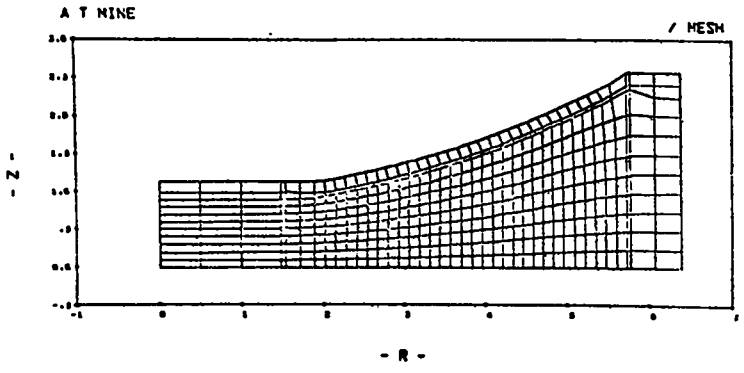

Fig. 8. Finite element mesh of antitank mine.

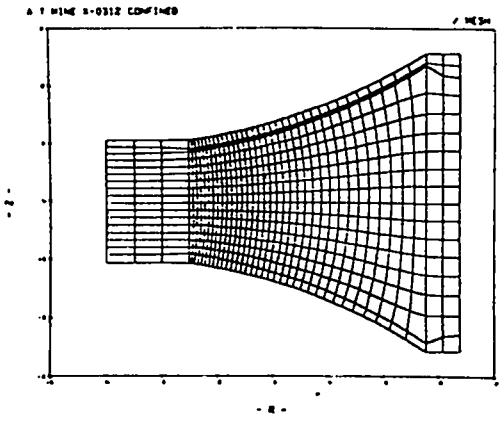

Fig. 9. Finite element mesh of full antitank mine.

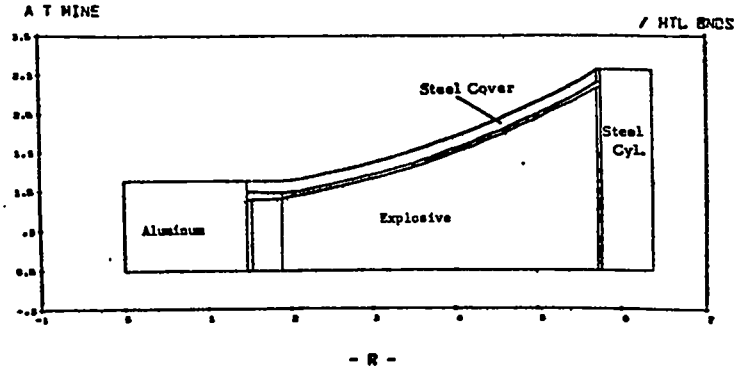

Fig. 10. Material boundaries of antitank mine.

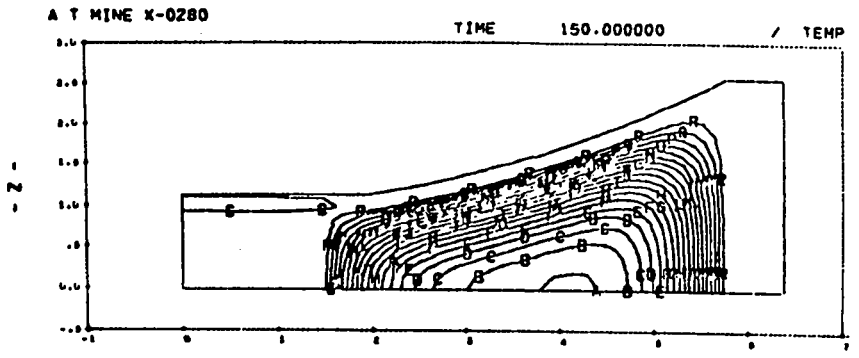

ID	Temp (°C)	ID	Temp (°C)
A	-51	J	-13
B	-47	K	-9
C	-43	L	-4
D	-38	M	0
E	-34	N	4
F	-30	O	9
G	-26	P	13
H	-21	Q	17
I	-17	R	21
		S	26

Fig. 11. Temperature gradients in unconfined configuration.

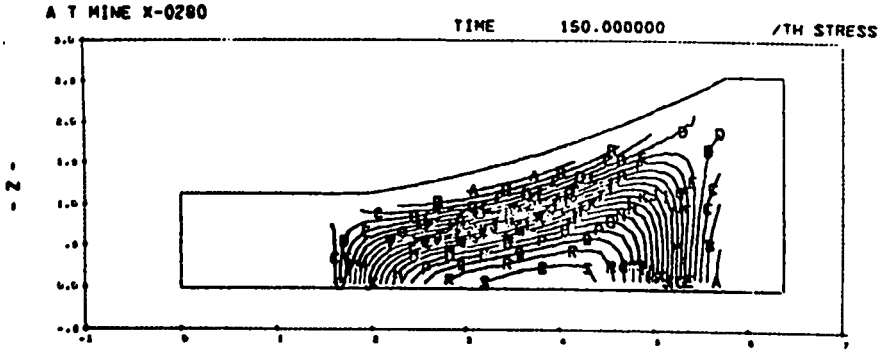

ID	Stress (MPa)	ID	Stress (MPa)
A	-23.0	K	5.7
B	-20.1	L	8.6
C	-17.2	M	11.5
D	-14.5	N	14.5
E	-11.5	O	17.2
F	-8.6	P	20.1
G	-5.7	Q	23.0
H	-2.9	R	25.9
I	0.0	S	28.7
J	2.9		

Fig. 12. Circumferential stress contours in X-0280.

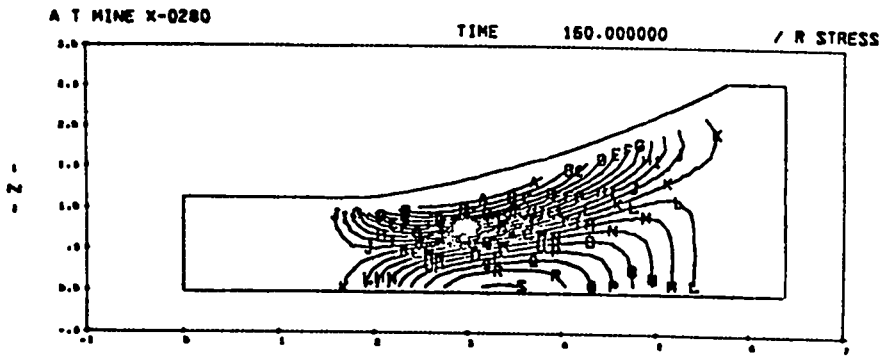

ID	Stress (MPa)	ID	Stress (MPa)
A	24.3	K	0.0
B	21.8	L	2.4
C	19.4	M	4.8
D	17.0	N	7.3
E	14.6	O	9.7
F	12.1	P	12.1
G	-9.7	Q	14.6
H	-7.3	R	17.0
I	-4.8	S	19.4
J	-2.4		

Fig. 13. Radial stress contours in X-0280.

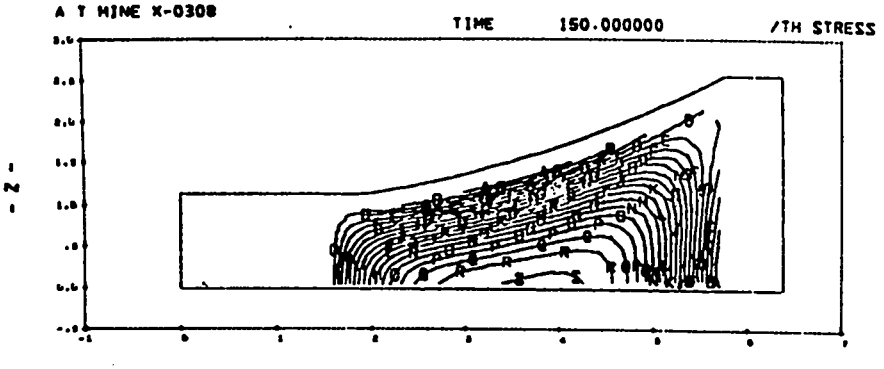

ID	Stress (MPa)	ID	Stress (MPa)
A	-8.7	K	1.0
B	-7.7	L	1.9
C	-6.8	M	2.9
D	-5.8	N	3.9
E	-4.8	O	4.8
F	-3.9	P	5.8
G	-2.9	Q	6.8
H	-1.9	R	7.7
I	-1.0	S	8.7
J	0.0		

Fig. 14. Circumferential stress contours in X-0308.

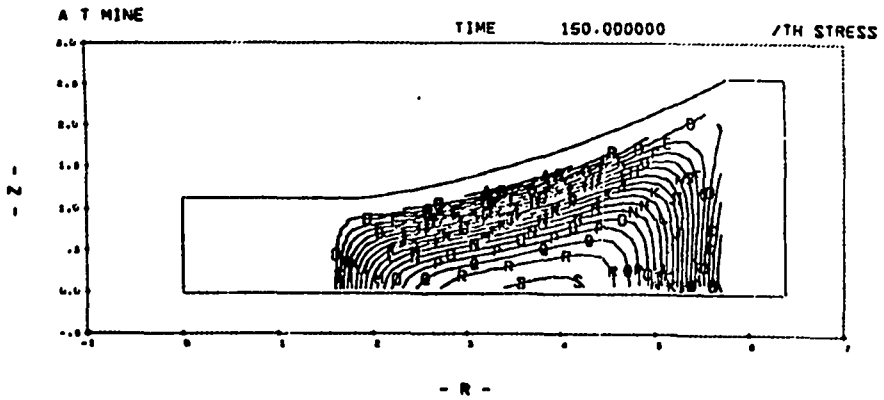

ID	Stress (MPa)	ID	Stress (MPa)
A	-12.0	K	1.3
B	-10.6	L	2.7
C	-9.3	M	4.0
D	-8.0	N	5.3
E	-6.6	O	6.6
F	-5.3	P	8.0
G	-4.0	Q	9.3
H	-2.7	R	10.6
I	-1.3	S	12.0
J	0.0		

Fig. 15. Circumferential stress contours in X-0312.

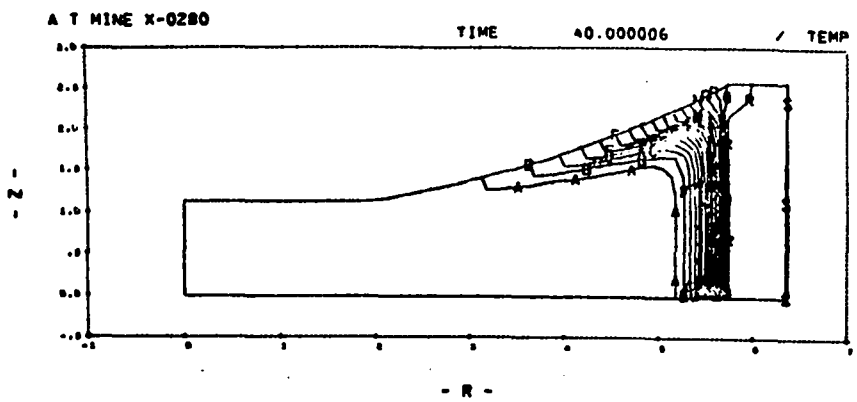

ID	Temp (°C)	ID	Temp (°C)
A	-50	K	-8
B	-46	L	-4
C	-42	M	0
D	-37	N	4
E	-33	O	8
F	-29	P	12
G	-25	Q	17
H	-21	R	21
I	-17	S	25
J	-12		

Fig. 16. X-0280 temperature gradients in confined configuration.

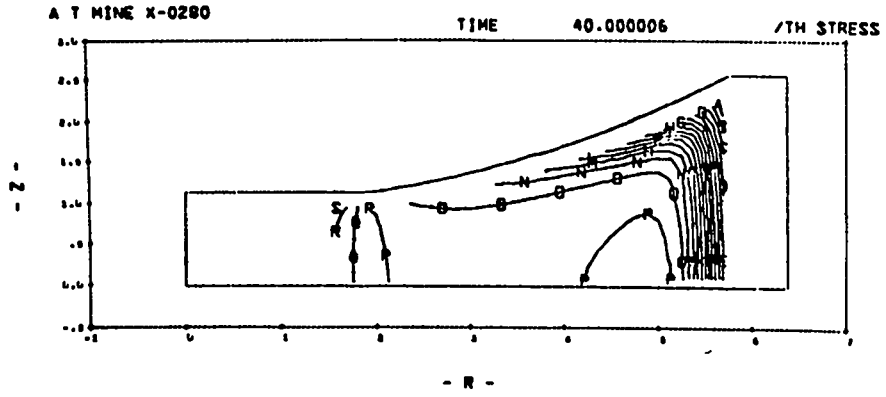

ID	Stress (MPa)	ID	Stress (MPa)
A	-5	K	45
B	0	L	50
C	5	M	55
D	10	N	60
E	15	O	65
F	20	P	70
G	25	Q	75
H	30	R	80
I	35	S	85
J	40		

Fig. 17. Circumferential stress contours in X-0280.

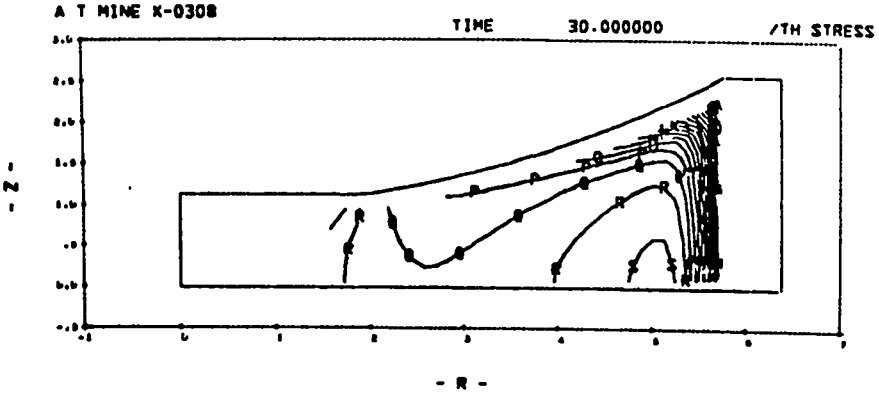

ID	Stress (MPa)	ID	Stress (MPa)
A	0.0	K	14.2
B	1.4	L	15.6
C	2.9	M	17.0
D	4.3	N	18.4
E	5.7	O	19.8
F	7.1	P	21.2
G	8.5	Q	22.7
H	9.9	R	24.1
I	11.4	S	25.5
J	12.8		

Fig. 18. Circumferential stress contours in X-0308.

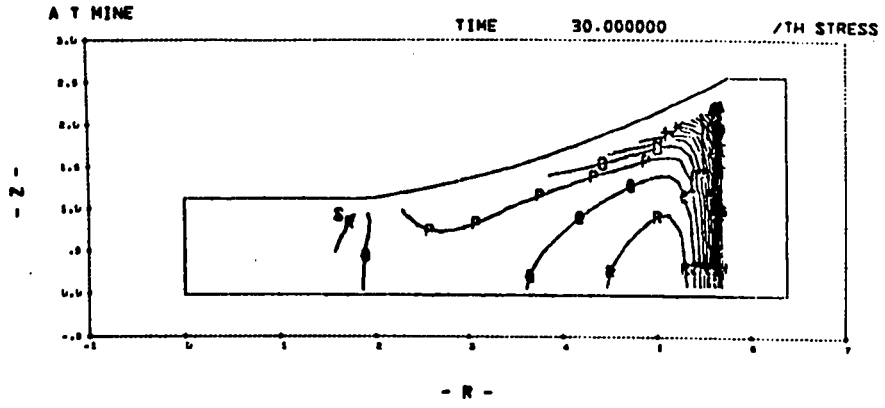

ID	Stress (MPa)	ID	Stress (MPa)
A	0.0	K	17.5
B	1.8	L	19.3
C	3.5	M	21.0
D	5.3	N	22.8
E	7.0	O	24.5
F	8.8	P	26.3
G	10.5	Q	28.0
H	12.3	R	29.8
I	14.0	S	31.5
J	15.8		

Fig. 19. Circumferential stress contours in X-0312.

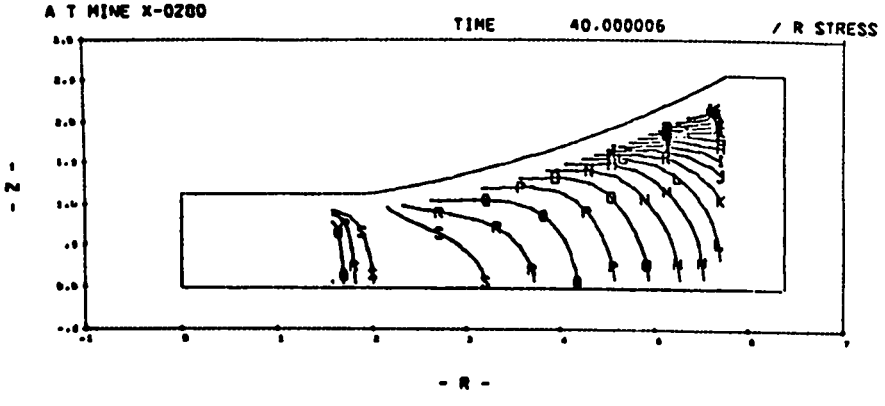

ID	Stress (MPa)	ID	Stress (MPa)
A	-8.9	K	35.4
B	-4.5	L	39.8
C	0.0	M	44.2
D	4.5	N	48.6
E	8.9	O	53.0
F	13.3	P	57.4
G	17.7	Q	61.8
H	22.1	R	66.3
I	26.5	S	70.7
J	30.9		

Fig. 20. Radial stress contours in X-0280.

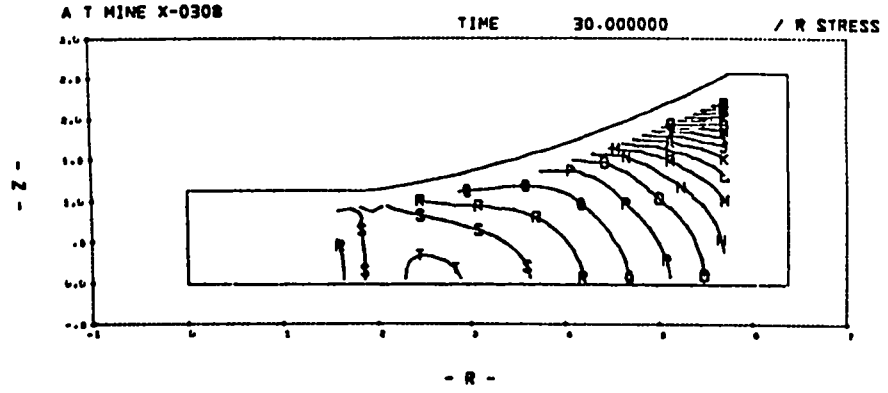

ID	Stress (MPa)	ID	Stress (MPa)
A	0.0	K	14.2
B	1.5	L	15.6
C	2.9	M	17.0
D	4.3	N	18.4
E	5.7	O	19.8
F	7.1	P	21.3
G	8.5	Q	22.7
H	9.9	R	24.1
I	11.4	S	25.5
J	12.8		

Fig. 21. Radial stress contours in X-0308.

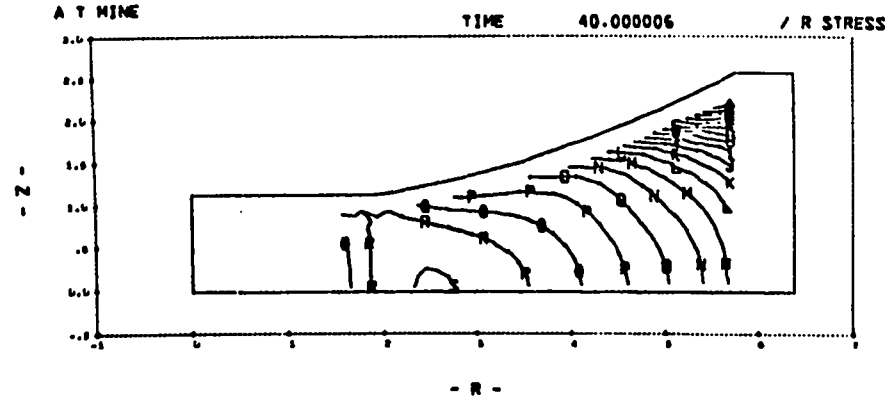

ID	Stress (MPa)	ID	Stress (MPa)
A	0.0	K	17.8
B	1.7	L	19.6
C	3.5	M	21.4
D	5.3	N	23.2
E	7.1	O	25.0
F	8.9	P	26.7
G	10.7	Q	28.5
H	12.5	R	30.3
I	14.2	S	32.1
J	16.0		

Fig. 22. Radial stress contours in X-0312.

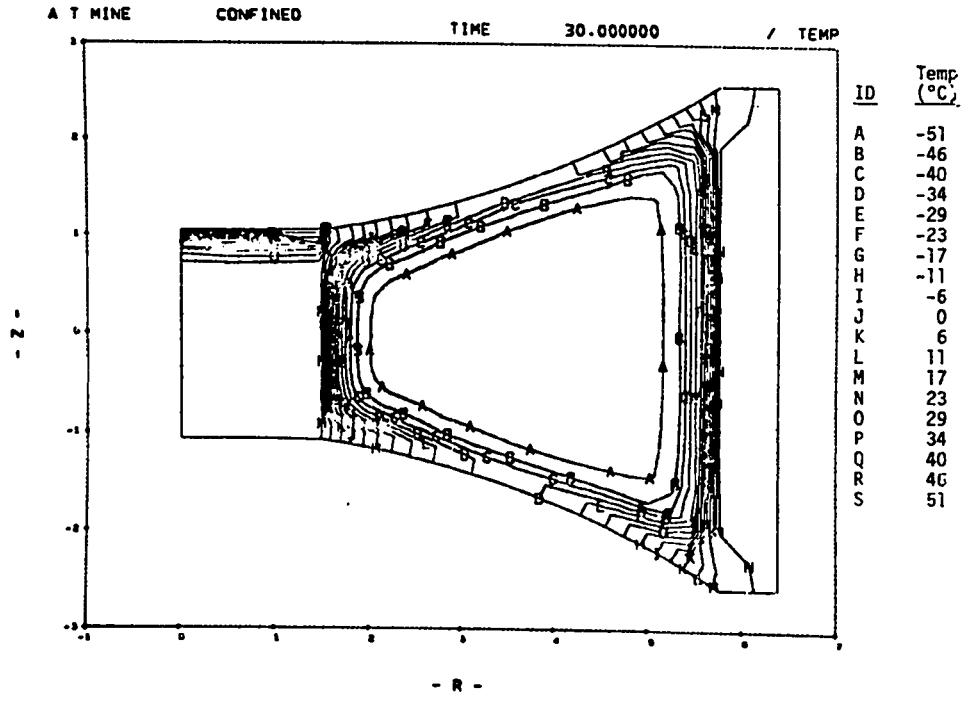

Fig. 23. Temperature gradients in confined configuration with unbonded cover.

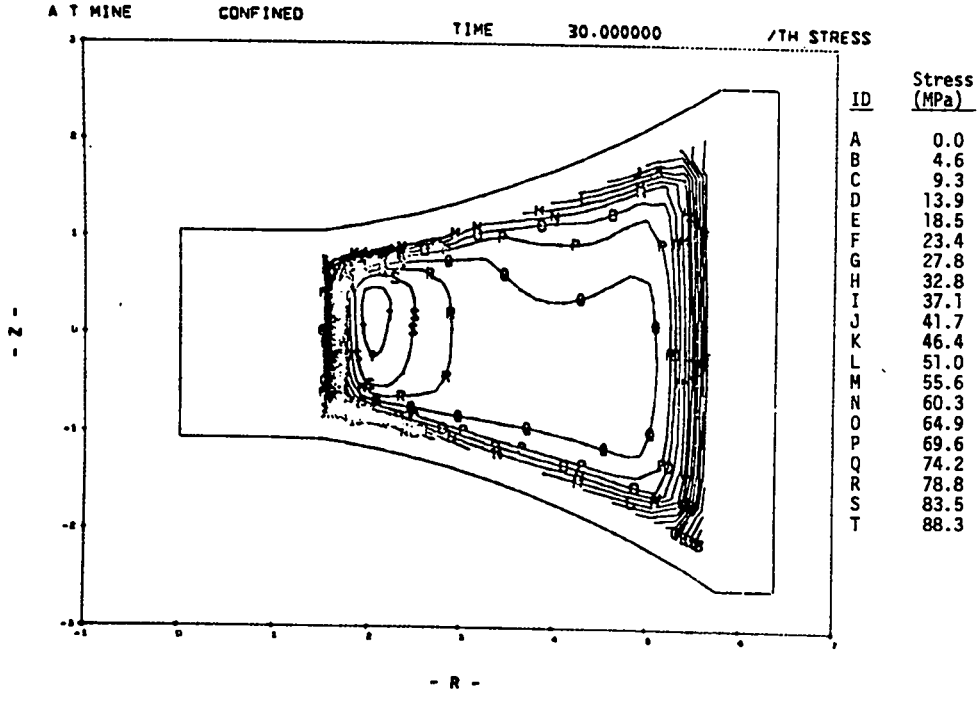

Fig. 24. Circumferential stress contours in X-0280.

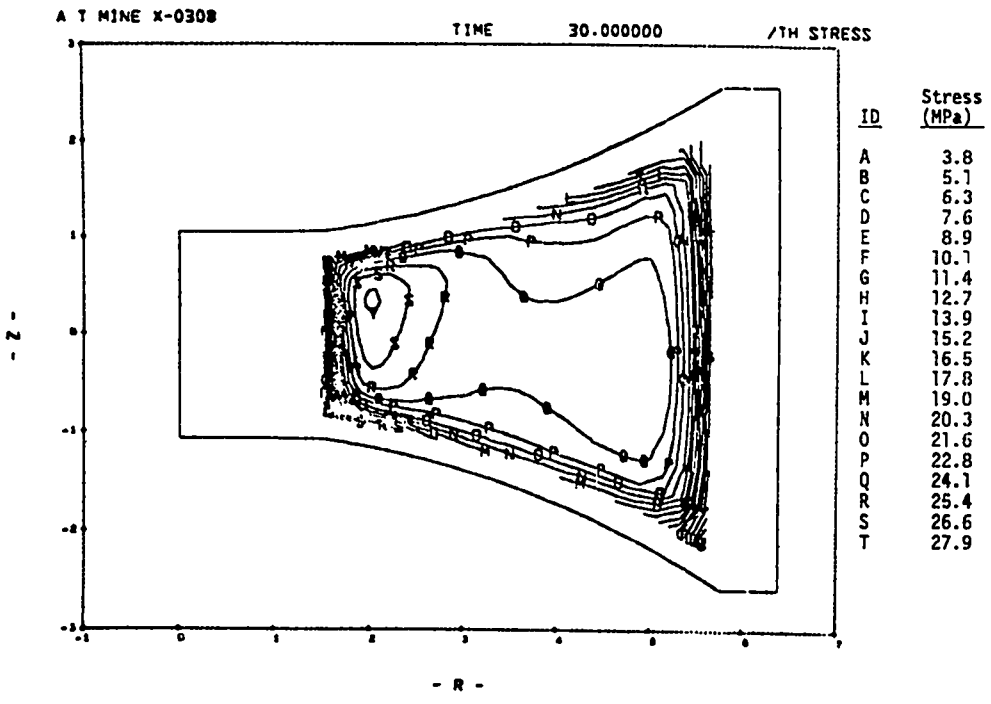

Fig. 25. Circumferential stress contours in X-0308.

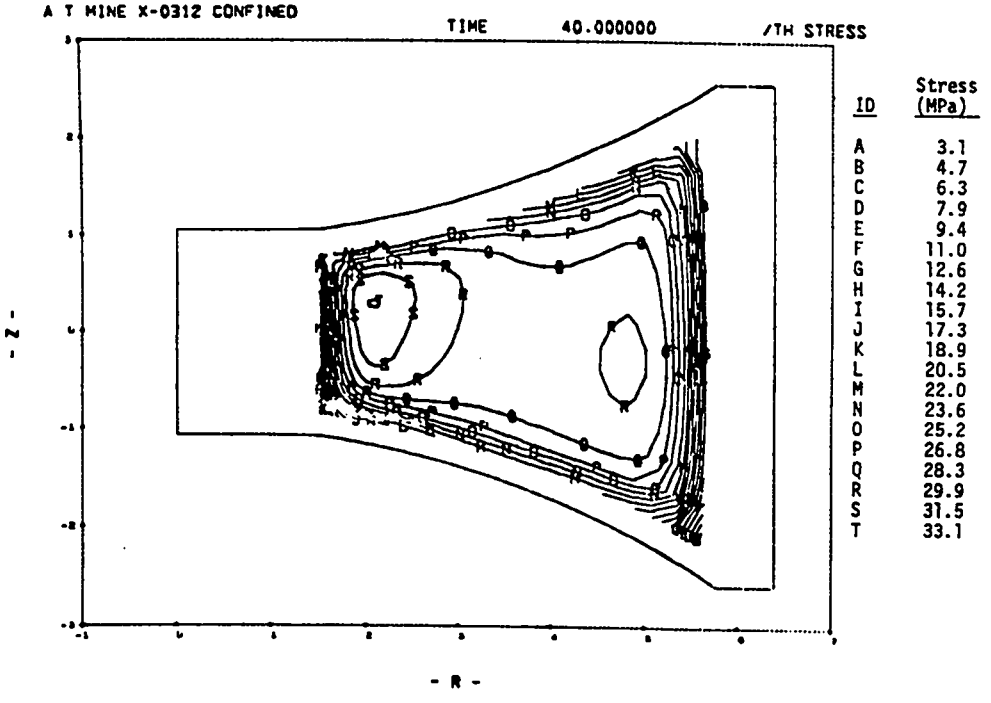

Fig. 26. Circumferential stress contours in X-0312.

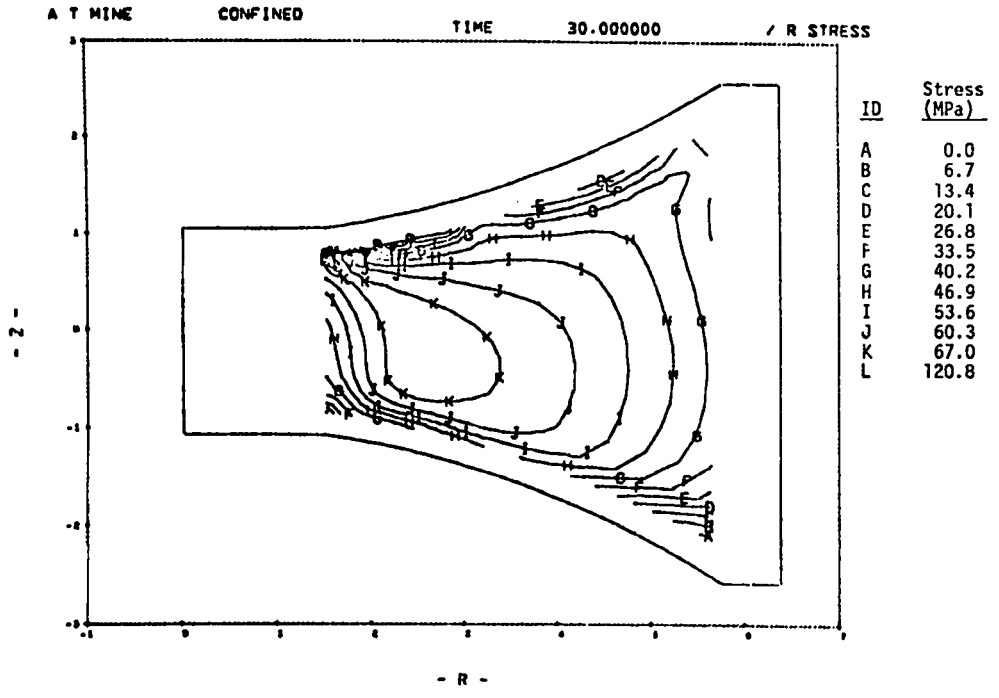

Fig. 27. Radial stress contours in X-0280.

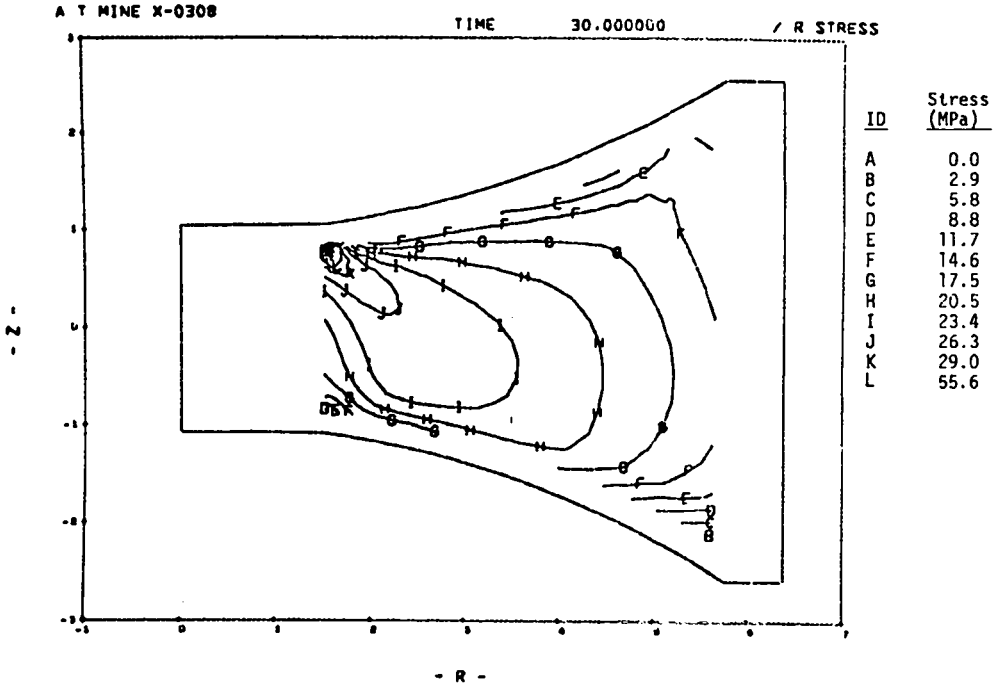

Fig. 28. Radial stress contours in X-0308.

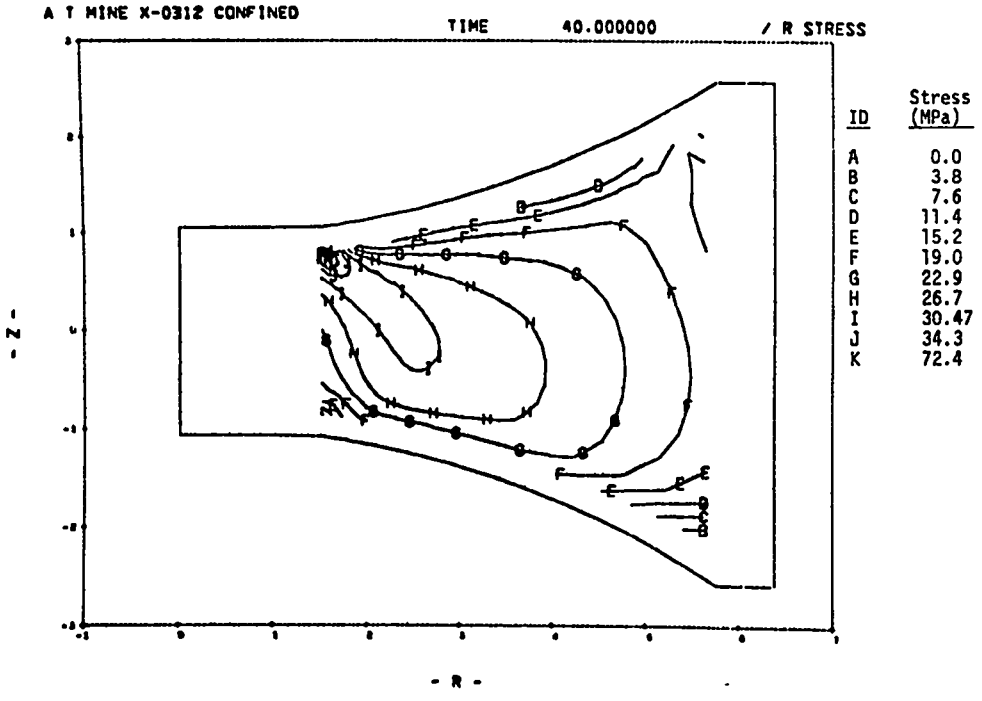

Fig. 29. Radial stress contours in X-0312.